JOM, Vol. 68, No. 10, 2016
DOI: 10.1007/s11837-016-2068-x

High-Throughput Computational Screening of Electrical and Phonon Properties of Two-Dimensional Transition Metal Dichalcogenides

IZAAK WILLIAMSON,[1,4] ANDRES CORREA HERNANDEZ,[1] WINNIE WONG-NG,[2] and LAN LI[1,3]

1.—Micron School of Materials Science and Engineering, Boise State University, Boise, ID 83725, USA. 2.—Materials Measurement Division, National Institute of Standards and Technology, Gaithersburg, MD 20899, USA. 3.—Center for Advanced Energy Studies, Idaho Falls, ID 83401, USA. 4.—e-mail: izaakwilliamson@u.boisestate.edu

Two-dimensional transition metal dichalcogenides (2D-TMDs) are of broadening research interest due to their novel physical, electrical, and thermoelectric properties. Having the chemical formula MX_2, where M is a transition metal and X is a chalcogen, there are many possible combinations to consider for materials-by-design exploration. By identifying novel compositions and utilizing the lower dimensionality, which allows for improved thermoelectric performance (e.g., increased Seebeck coefficients without sacrificing electron concentration), MX_2 materials are promising candidates for thermoelectric applications. However, to develop these materials into wide-scale use, it is crucial to comprehensively understand the compositional affects. This work investigates the structure, electronic, and phonon properties of 18 different MX_2 materials compositions as a benchmark to explore the impact of various elements. There is significant correlation between properties of constituent transition metals (atomic mass and radius) and the structure/properties of the corresponding 2D-TMDs. As the mass of M increases, the n-type power factor and phonon frequency gap increases. Similarly, increases in the radius of M lead to increased layer thickness and Seebeck coefficient S. Our results identify key factors to optimize MX_2 compositions for desired performance.

INTRODUCTION

Transition metal dichalcogenides (TMDs), having the chemical formula MX_2 (M = transition metal, X = chalcogen, i.e., S, Se, Te), have received attention over the years for having interesting magnetic[1,2] and photoelectric[3] properties. Bulk three-dimensional transition metal dichalcogenides (3D-TMDs) can exist as layered structures wherein each layer consists of a transition metal (M) sheet sandwiched between two chalcogen (X) sheets. These layers exist in one of two structure types: 2H-type having D_{6h} point group symmetry and 1T-type having D_{3d} point group symmetry. Strong covalent bonding exists *within* the MX_2 layers (along the a and b axes) while much weaker van der Waals (vdW) interactions exist *between* the layers (along the c axis). This allows individual MX_2 layers to be separated via mechanical exfoliation.[4] The separated 2D-TMD materials have recently attracted much interest for a variety of applications including electronics,[5–9] optoelectronics,[10–13] catalysis,[14,15] and thermoelectrics.[16–19] Thermoelectrics convert waste heat into electric power, governed by figure-of-merit $ZT = S^2\sigma T/k$, where S is the Seebeck coefficient, σ is the electrical conductivity, $S^2\sigma$ is the power factor, T is the temperature, and k is the thermal conductivity. Common thermoelectric materials include clathrates,[20] half-Heusler alloys,[21] and skutterudites.[22–25] Reduced dimensionality offers the potential for smaller device features and has been shown to greatly reduce short-channel effects, increase the on–off ratio, and reduce switching voltage in field-effect transistors (FET).[7,10] In addition, the quantum confinement effect and sharp features in the electronic density of states (DoS) are

(Published online August 8, 2016)

beneficial for greatly improving thermoelectric properties, such as increasing the Seebeck coefficient, S, in 2D-TMDs compared to that of the bulk structures.[26–28] It is also predicted that the lower dimensionality increases diffusive boundary scattering, effectively reducing the thermal conductivity, k. Lowering the dimensionality of Si, for example, has shown strong reductions in thermal conductivity and implications for enhanced thermoelectric performance.[29,30] Each of these factors contribute to the strong motivation for further understanding the behavior of 2D-TMDs.

With a large number of potential 2D-TMD compounds, it is important to identify key structure–property–performance relationships in order to screen preferred materials. A few studies have been performed to analyze the stability and electronic structure of 2D-TMDs and -TMOs (transition metal dioxides) using density functional theory (DFT).[5,6] These offer a general analysis of trends across a broad range of compositions and identify most structures to be semiconducting with small indirect band gaps. Rasmussen et al.[6] found that only CrX_2, MoX_2, and WX_2 systems exhibit direct band gaps. From these works, it is useful to identify more favorable 2D-TMD compositions in terms of stability, electrical properties, and optical properties. However, none have been directed at what compositions are possible. Graedel et al.[31] developed a method for quantifying the environmental implications, supply risk, and vulnerability to supply restrictions for 62 transition metals and metalloids. These "criticality scores" can be used to identify preferred materials and narrow the focus for screening potential compositions in order to develop high-performance, cost-effective, and environmentally friendly materials.

In this work, we use existing stability reference data in conjunction with criticality scores to identify transition metals and resulting 2D-TMD compounds to represent a narrowed scope of feasible options for MX_2 materials screening purposes. A list of six transition metals was selected to offer a range of common oxidation states, atomic masses, and atomic radii. Combined with three chalcogens—S, Se, and Te—this amounted to 18 total compounds. The geometries, electrical properties, and phonon properties of these compounds were investigated through first-principles calculation and analyzed with respect to physical properties of the transition metals. This unique approach offers a means of identifying general trends in constituent elements in order to predict structure–properties–performance relationships in resulting 2D-TMDs.

COMPUTATIONAL METHODS

Structural and electronic structure calculations were conducted using the projector augmented wave (PAW) method[32,33] within the framework of DFT via the Vienna ab initio simulation package (VASP) code.[34] The Perdew–Burke–Ernzerhof (PBE)[35] formalism was employed within the spin-dependent generalized gradient approximation (GGA). A plane-wave expansion cutoff of 500 eV was used along with an automatic Γ-centered $12 \times 12 \times 1$ k-point mesh Brillouin zone integration for the initial geometry optimizations. A Gaussian smearing of 0.025 eV was used to account for Fermi surface broadening while atomic positions and basis vectors were relaxed to within 0.01 eV/Å. To avoid image interaction, MX_2 sheets were separated by a distance >20 Å. After geometry optimizations, the electronic structure calculations were performed with an increased k-point mesh of $24 \times 24 \times 1$ while strong correlation effects were accounted for using the DFT + U scheme for all transition metals. The on-site Coulomb potentials of U = 4.38 eV, 8.0 eV, 3.0 eV, 8.0 eV, 6.0 eV, and 8.0 eV were used for Mo, Ni, Sc, Ti, V, and W, respectively.[36] The on-site exchange potential J = 1.0 eV, was used for all metals.

Force constants used to estimate phonon properties were calculated using density functional perturbation theory (DFPT) following the method of Parlinski–Li–Kawazoe.[37] To calculate the real-space force constants, long-range effects were accounted for by using a converged supercell size of $3 \times 3 \times 2$ and a corresponding k-point mesh of $4 \times 4 \times 2$. The resulting force constants were used to generate phonon DoS and partial phonon DoS.[38]

In bulk TMD structures, it is necessary to employ vdW corrections to account for the inter-sheet interactions as they are determined to be largely controlled by vdW forces. Indeed, our own comparison of bulk MoS_2 (using the Grimme DFT-D2 method[39] and a $12 \times 12 \times 4$ k-point mesh) with that of reported experimental values[40] revealed that accounting for vdW forces increases the accuracy by about 24.5% and 11.9% for sheet separation distance and cell volume, respectively. However, since the bonding within the 2D-TMD sheets is primarily strong covalent bonding, it may not be necessary to include such corrections for calculations involving the isolated sheets. We tested for 2D-MoS_2 and found that incorporating vdW corrections gave the same lattice constant and layer thickness values (to within 0.3% error) yet produced an *indirect* band gap of 1.65 eV. Since 2D-MoS_2 is known to be a *direct* band gap semiconductor, it would seem that DFT-D2-based vdW corrections actually have a negative impact on 2D-TMD systems. Due to the minimal difference in geometry and potential error in the electronic structure calculations, we did not employ vdW in this work.

RESULTS AND DISCUSSION

Structure Screening

The unique physical, electrical, and thermal properties of 2D-MX_2s are of great research interest for a wide range of applications. However, there are many possible MX_2 combinations to consider. Work by Graedel et al. highlights the "criticality scores"

for transition metals, allowing for the comparison of three important factors to consider for materials design: environmental implications, supply risk, and vulnerability to supply restrictions.[31] By comparing this list with the stability results from Ataca et al.[5] and Rasmussen et al.,[6] we have narrowed the list of favorable transition metals to six: Mo, Ni, Sc, Ti, V, and W. These metals offer a broad range of atomic masses (44.96–183.85 u),[41] atomic radii (0.62–0.885 Å),[42] and most common oxidation state (+2 to +6). The comparison of the calculated properties with regard to these factors offers an effective approach towards identifying key relationships between constituent elements and desired structural, electrical, and thermal properties.

The complete list of 18 2D-TMDs used in this study is given in Table I. The most common oxidation state, atomic mass, and atomic radius are listed for each transition metal (M). The resultant TMD consists of the corresponding chalcogen having either 2H- or 1T-type phase. The TMD lattice parameters, a, are typically similar to the layer thicknesses with the exception of ScS_2 and the NiX_2 system (with layer thicknesses about 1 Å smaller than a). Also, both the lattice parameter and layer thickness increase with X's atomic number. The range of values for both the lattice parameter and layer thickness noticeably decreases with increasing oxidation state of the transition metal. Similarly, this range also decreases with increasing atomic mass of the transition metal down to a range less than 0.5 Å for both the MoX_2 and WX_2 systems (m_{Mo} = 95.94 u, m_W = 183.85 u). Figure 1 shows how the lattice parameter and layer thickness of the resulting 2D-TMD are influenced by the atomic mass and atomic radius of the constituent transition metal. Interestingly, the layer thickness increases with atomic radius of the transition metal while the lattice parameter remains constant. The results reveal some materials design principles that lattice mismatch—causing a large instability in the formation of heterostructures—is minimal or negligible, even though 2D-TMDs have large layer thickness differences.

Electrical Property Screening

Electronic structure calculations were performed for the 2D-TMDs and determined that many of the systems exhibit semiconducting behavior. The MoX_2, TiX_2, and WX_2 systems all have nonzero band gaps with Fermi levels just above their respective valence band maxima (VBM). The magnitude for each band gap decreases with X's increasing atomic number. Specifically, the MoX_2 and WX_2 systems have band gaps similar to each other, and they are the only systems with direct band gaps. These results are consistent with the findings of Rasmussen et al.[6] In contrast, the NiX_2, ScX_2, and VX_2 systems all exhibit p-type semi-conducting behavior with Fermi levels below the VBM. The only member of the VX_2 system with a mid-gap Fermi level is VSe_2—a semiconductor with an indirect band gap of 0.72 eV. Generally speaking, the compounds exhibiting the largest band gaps are the ones that involve mid-level transition metal radii. The most conductive compounds have either very large (Sc) or very small (Ni) atomic radii. It implies a Gaussian distribution of band gaps across the range of atomic radii.

To further investigate electrical properties, the thermoelectric power factor $S^2\sigma$ and Seebeck coefficient S were also calculated for each TMD. The Boltzmann transport equation (BTE) was solved in order to calculate semi-classic transport coefficients.[43] The Seebeck coefficients are shown in Fig. 2 as a function of carrier concentration. Each calculation was evaluated for the temperature of 300 K. Consistent with the band gaps, the MoX_2, TiX_2, and WX_2 systems show the largest-magnitude S values (nearly 1000 μV/K for the given carrier concentration range) while the other systems produced much smaller values (<50 μV/K). Also, the MoX_2 and WX_2 systems yield similar plots for all cases except the n-type S calculation for the MTe_2 structures (see Fig. 2f). The $TiTe_2$ results show a noticeable peak in the Seebeck coefficient of about (450–500) μV/K for both p- and n-type calculations. It suggests a bipolar conduction for carrier concentrations below 10^{11} e/cm^2 and an optimum S value for this system. This bipolar effect could cause degradation in the thermoelectric performance.

The Seebeck values S were combined with electrical conductivity (σ/τ) calculations, and using the constant relaxation time approximation, the power factor was calculated as $S^2\sigma$.[44,45] The choice of relaxation time (τ) comes from the work of Kaasbjerg et al.[46] who used DFT to calculate the effective electron mass ($m^* = 0.48\ m_e$) and electron mobility in single-layer MoS_2. At 300 K, and for carrier densities between 10^{11} and 10^{13} cm^{-2}, they calculated an electron mobility of about $\mu = 400$ cm^2 V^{-1} s^{-1}. Using the equation $\mu = \frac{q}{m^*}\tau$, where q is the electronic charge, the average relaxation time equates to about $\tau \approx 10^{-13}$ s. This value was used for each system and the resulting first-peak maximum power factor values are given in Table II. The n-type results indicate a correlation between the magnitude of the power factor and the mass of the constituent transition metal. The heaviest metals, W and Mo, produce the largest power factors of 7.90×10^{-3} and 5.82×10^{-3} W/m/K^2, respectively, while the lightest metal, Sc, has the smallest power factors (0.78–1.39) $\times 10^{-3}$ W/m/K^2. The type of chalcogen does not have a large impact on the power factor of the resultant TMD. For example, the TiX_2 system has a range of only 0.04×10^{-3} W/m/K^2. This could be useful for design purposes, where necessary restrictions on the use of chalcogen would likely not affect the overall performance of the material. The p-type power factor

Table I. Oxidation state, atomic mass (u), and atomic radius (Å) for each transition metal

M	Oxidation state	Atomic mass[a] (u)	Atomic radius[b] (Å)	*X*	Type	*a* (Å)	*t* (Å)	E_g (eV)
Mo	+6	95.94	0.79	S	2H	3.182	3.128	1.69
				Se	2H	3.319	3.338	1.46
				Te	2H	3.549	3.611	1.10
Ni	+2	58.69	0.62	S	1T	3.351	2.336	0.01
				Se	1T	3.545	2.479	–
				Te	2H	3.720	2.927	–
Sc	+3	44.956	0.885[c]	S	2H	3.777	2.708	1.72[d]
				Se	2H	3.512	3.635	–
				Te	2H	3.728	4.009	–
Ti	+4	47.88	0.745	S	1T	3.398	2.854	1.18
				Se	2H	3.485	3.239	0.92
				Te	2H	3.736	3.571	0.30
V	+5	50.942	0.72	S	1T	3.174	2.938	–
				Se	2H	3.335	3.197	0.72
				Te	2H	3.596	3.502	0.02
W	+6	183.85	0.80	S	2H	3.181	3.139	1.85
				Se	2H	3.317	3.355	1.58
				Te	2H	3.552	3.623	1.07

The 2D-TMDs (MX_2), consisting of a transition metal (M) and chalcogen (X), have either 2H- or 1T-type structures. Lattice parameter a (Å), layer thickness t (Å), and electronic band gap E_g (eV) of the corresponding TMD are also given.[a]Reference 40.[b]Reference 41. Values taken from list of crystal radii with +4 charge and six-fold coordination.[c]Value for +3 charge.[d]E_F sits on mid-gap state.

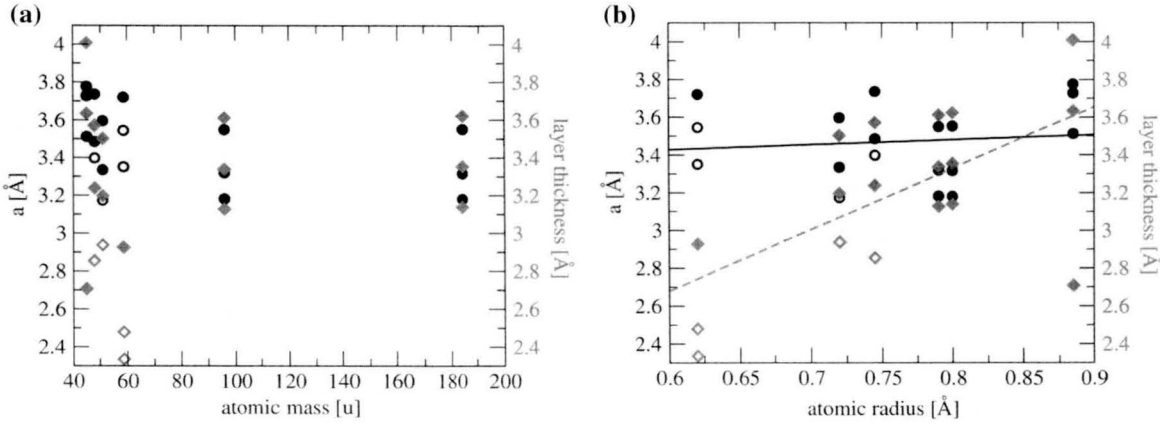

Fig. 1. Effects of (a) atomic mass and (b) atomic radius of the transition metal on the lattice constant, *a*, and layer thickness of the resulting 2D-TMD structure. Circles and diamonds refer to lattice constant and layer thickness values, respectively. Open and filled data points refer to 1T- and 2H-type MX_2 structures, respectively. Solid and dashed linear trend lines have been added to plot (b) to guide the eye for lattice constant and layer thickness data, respectively.

results, however, are not as consistent. Many of the systems exhibit large dependence on the type of chalcogen used. For example, the NiX_2 system has a range of values exceeding 7.83×10^{-3} W/m/K^2.

Phonon Property Screening

A thorough understanding of heat transfer is important for device design. In particular, 2D-TMDs have attracted much interest in this regard for the unique transport of thermal energy at the low dimension. Developing high-performance thermoelectric materials, for example, requires a large figure-of-merit, ZT which is dependent upon having low thermal conductivity. Thermal conductivity calculations involve a detailed investigation of the Boltzmann transport equation, namely second- and third-order solutions to account for both normal and umklapp phonon modes. Here, we focus primarily on phonon DoS calculations as a means of qualitatively comparing phonon properties for 2D-TMDs in order to identify trends. Figure 3 shows the projected phonon DoS calculation results for the MS_2 system. The total phonon DoS is shown with a

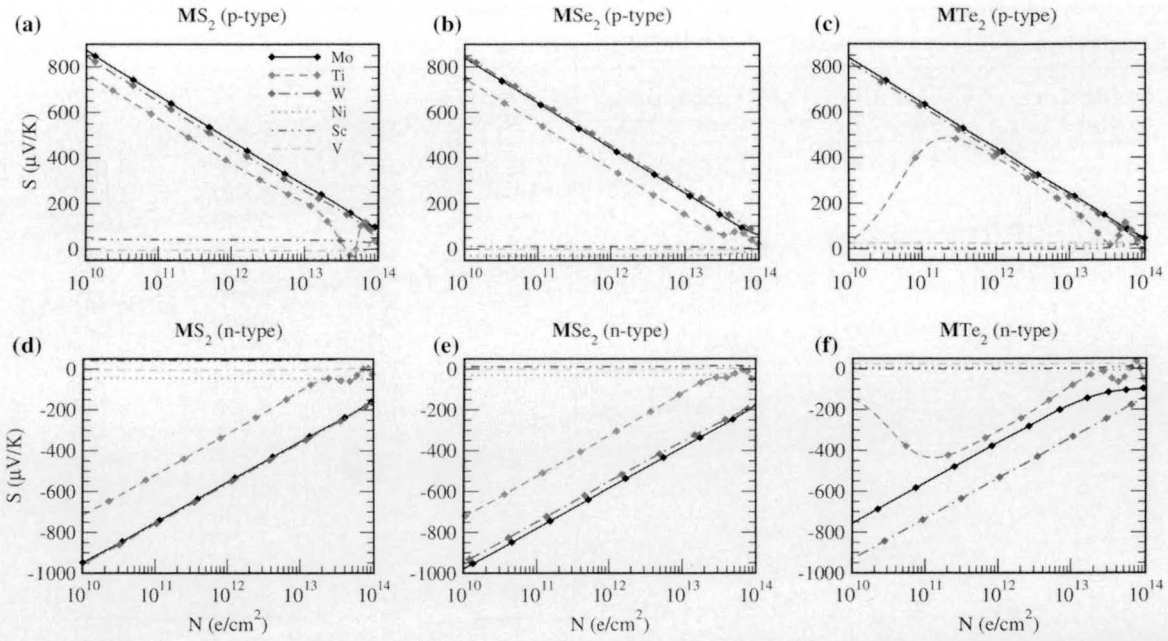

Fig. 2. Seebeck coefficient S (μV/K) calculated as a function of carrier concentration N (e/cm^2) for 2D-TMDs. Plots (a)–(c) show the p-type S values while plots (d)–(f) depict n-type values. The first (a, d), second (b, e), and third (c, f) columns compare the MS_2, MSe_2, and MTe_2 systems, respectively. The MoX_2, TiX_2, and WX_2 systems all exhibit semiconducting behavior and are distinguished by lines with diamonds (Mo diamonds–solid line, Ti diamonds–dashed line, and W diamonds–dot-dashed line). The more-conductive NiX_2, ScX_2, and VX_2 systems all exhibit low S values and are depicted using lines (Ni dotted line, Sc dot–dot-dashed line, and V dash–dash-dotted line). All calculations were performed at the temperature of 300 K.

Table II. Power factor ($S^2\sigma$) values for the 18 2D-TMDs

			$S^2\sigma*10^{-3}$ (W/m/K^2)	
M	***X***	**Type**	***n*-type**	***p*-type**
Mo	S	2H	5.82	5.09
	Se	2H	5.49	3.70
	Te	2H	5.26	3.26
Ni	S	1T	3.36	8.62
	Se	1T	2.97	0.79
	Te	2H	0.45	3.03
Sc	S	2H	1.16	0.75
	Se	2H	1.39	0.96
	Te	2H	0.78	2.81
Ti	S	1T	2.07	9.32
	Se	2H	2.11	3.16
	Te	2H	2.10	6.05
V	S	1T	1.29	0.86
	Se	2H	5.18	1.68
	Te	2H	4.25	0.79
W	S	2H	7.39	5.14
	Se	2H	7.90	5.05
	Te	2H	6.10	4.21

Values are reported as 10^3 times larger than actual for the purpose of clarity in the table. Each value, when multiplied by 10^{-3}, yields units of W/m/K^2. These are calculated at 300 K for both n- and p-type.

solid line in each case while contributions from the transition metal and sulfur atoms are represented by dash-dot and dashed lines, respectively. Figure 3a–f lists each MS_2 in order of increasing atomic mass of the constituent transition metal. As the mass difference between transition metal and

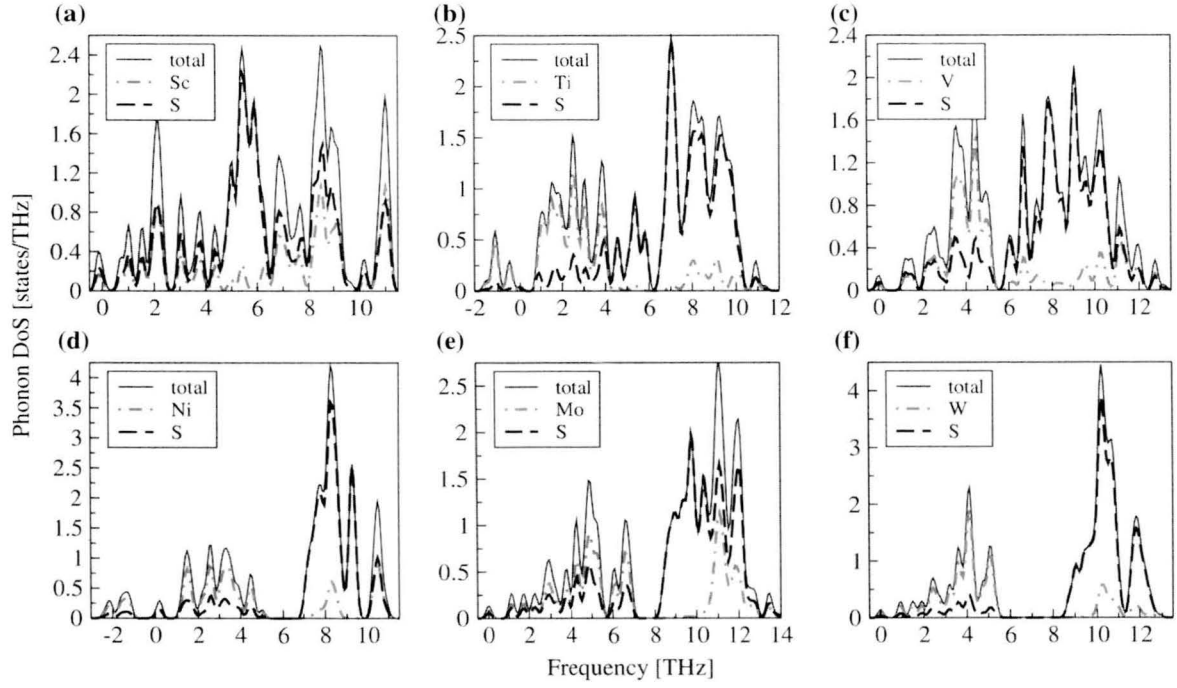

Fig. 3. Projected phonon DoS for each member of the MS_2 system. Each plot depicts the total phonon DoS with a solid line, the contribution from the transition metal with a dot-dashed line, and the contribution from the S atoms with a dashed line. Plots (a)–(f) are shown in order of increasing atomic mass of the transition metal as follows (a) ScS_2, (b) TiS2, (c) VS_2, (d) NiS_2, (e) MoS_2, and (f) WS_2.

sulfur atoms (32.066 u) increases, the frequency gap between the acoustic and optical phonon bands roughly increases. It suggests that, although mass difference can be beneficial for increased phonon scattering (and therefore decreased thermal conductivity), there might be an optimum mass difference before the different modes no longer scatter one another. If the mass difference is too large, the impurity (or defect) scattering term decreases. The WS_2 results, for example, have the largest mass difference (151.784 u) and consequently show the least amount of overlap between M and S modes. Such features imply minimal phonon scattering and thus a larger thermal conductivity k. It has been evidenced by Gu et al. that WS_2 does indeed have a larger thermal conductivity k than that of MoS_2.[19] In addition, their results reveal a monotonically increasing lattice thermal conductivity with increasing acoustic-optical frequency band gap. Sc, Ti, and V sulfides have negligibly small frequency gaps while Ni, Mo, and W sulfides have substantial gaps. In this regard, Sc, Ti, and V sulfides should exhibit the lowest lattice thermal conductivity.

CONCLUSION

A list of 18 2D-TMD compounds, having the chemical formula MX_2 (M = Mo, Ni, Sc, Ti, V, W; X = S, Se, Te), were chosen based on their potential stability and on the criticality scores of the constituent transition metals. First-principles geometry, electrical property, and phonon property calculations were performed. The results were compared with features of the transition metals in order to identify predictive property trends. The atomic radius of the transition metal correlates with the 2D-TMD properties. While the layer thickness of the compounds increases linearly with the transition metal radius, the lattice parameter remains constant. The electronic band gaps of TMDs follow a Gaussian-like distribution across the range of transition metal radii wherein the smallest and largest constituent metals yield negligibly small band gaps. In contrast, the mid-sized metals yield band gaps of greater than 1 eV. MoX_2, TiX_2, and WX_2 compounds have the largest Seebeck coefficients, S. The $TiTe_2$ compound exhibits bipolar conduction behavior with a noticeable S peak of about 450–500 μV/K for both p- and n-type calculations. The atomic mass of constituent metals also affects the compound properties. The heaviest metals, W and Mo, produce the largest n-type power factors, $S^2\sigma$. Mass difference between transition metal and sulfur atom enlarges the frequency gap between acoustic and optical phonon bands, indicating decreased phonon scattering. The Sc, Ti, and V sulfides have the smallest mass differences and the largest interaction between the metal and S contributions to phonon DoS, so they should exhibit a lower lattice thermal conductivity than the other MX_2 compounds. Our work provides a new approach to draw correlation between physical properties of constituent transition metals and resultant 2D-TMDs.

ACKNOWLEDGEMENTS

The authors would like to thank Dr. Dave Estrada at Boise State for helpful discussions of the experiment, Ken Blair at Boise State for assistance with computing facilities, as well as Idaho National Laboratory's high performance computing (HPC) center for computing support.

REFERENCES

1. S. Ogawa, *J. Appl. Phys.* 50, 2308 (1979).
2. T. Shishidou, A.J. Freeman, and R. Asahi, *Phys. Rev. B* 64, 180401 (2001).
3. H. Tributsch, *Z. Naturforsch. A* 32, 972 (1977).
4. J.N. Coleman, M. Lotya, A. O'Neill, S.D. Bergin, P.J. King, U. Khan, K. Young, A. Gaucher, S. De, R.J. Smith, I.V. Shvets, S.K. Arora, G. Stanton, H.Y. Kim, K. Lee, G.T. Kim, G.S. Duesberg, T. Hallam, J.J. Boland, J.J. Wang, J.F. Donegan, J.C. Grunlan, G. Moriarty, A. Shmeliov, R.J. Nicholls, J.M. Perkins, E.M. Grieveson, K. Theuwissen, D.W. McComb, P.D. Nellist, and V. Nicolosi, *Science* 331, 568 (2011).
5. C. Ataca, H. Sahin, and S. Ciraci, *J. Phys. Chem. C* 116, 8983 (2012).
6. F.A. Rasmussen and K.S. Thygesen, *J. Phys. Chem. C* 119, 13169 (2015).
7. S.Z. Butler, S.M. Hollen, L.Y. Cao, Y. Cui, J.A. Gupta, H.R. Gutierrez, T.F. Heinz, S.S. Hong, J.X. Huang, A.F. Ismach, E. Johnston-Halperin, M. Kuno, V.V. Plashnitsa, R.D. Robinson, R.S. Ruoff, S. Salahuddin, J. Shan, L. Shi, M.G. Spencer, M. Terrones, W. Windl, and J.E. Goldberger, *ACS Nano* 7, 2898 (2013).
8. S. McDonnell, R. Addou, C. Buie, R.M. Wallace, and C.L. Hinkle, *ACS Nano* 8, 2880 (2014).
9. C. Gong, L. Colombo, R.M. Wallace, and K. Cho, *Nano Lett.* 14, 1714 (2014).
10. R. Ganatra and Q. Zhang, *ACS Nano* 8, 4074 (2014).
11. B. Radisavljevic, A. Radenovic, J. Brivio, V. Giacometti, and A. Kis, *Nat. Nanotechnol.* 6, 147 (2011).
12. O. Lopez-Sanchez, D. Lembke, M. Kayci, A. Radenovic, and A. Kis, *Nat. Nanotechnol.* 8, 497 (2013).
13. B.W.H. Baugher, H.O.H. Churchill, Y.F. Yang, and P. Jarillo-Herrero, *Nat. Nanotechnol.* 9, 262 (2014).
14. W. Chen, E.J.G. Santos, W.G. Zhu, E. Kaxiras, and Z.Y. Zhang, *Nano Lett.* 13, 509 (2013).
15. T.F. Jaramillo, K.P. Jorgensen, J. Bonde, J.H. Nielsen, S. Horch, and I. Chorkendorff, *Science* 317, 100 (2007).
16. W. Huang, H.X. Da, and G.C. Liang, *J. Appl. Phys.* 113, 104304 (2013).
17. W. Huang, X. Luo, C.K. Gan, S.Y. Quek, and G.C. Liang, *Phys. Chem. Chem. Phys.* 16, 10866 (2014).
18. C. Lee, J. Hong, M.H. Whangbo, and J.H. Shim, *Chem. Mater.* 25, 3745 (2013).
19. X.K. Gu and R.G. Yang, *Appl. Phys. Lett.* 105, 131903 (2014).
20. G.S. Nolas and G.A. Slack, *Am. Sci.* 89, 136 (2001).
21. M.M. Zou, J.F. Li, and T. Kita, *J. Solid State Chem.* 198, 125 (2013).
22. J.S. Dyck, W.D. Chen, C. Uher, L. Chen, X.F. Tang, and T. Hirai, *J. Appl. Phys.* 91, 3698 (2002).
23. J. Yang, W. Zhang, S.Q. Bai, Z. Mei, and L.D. Chen, *Appl. Phys. Lett.* 90, 192111 (2007).
24. I. Williamson, L.J.Y. Her, X.L. Su, Y.G. Yan, W. Wong-Ng, and L. Li, *J. Appl. Phys.* 119, 055101 (2016).
25. G.J. Tan, S.Y. Wang, H. Li, Y.G. Yan, and X.F. Tang, *J. Solid State Chem.* 187, 316 (2012).
26. L.D. Hicks and M.S. Dresselhaus, *Phys. Rev. B* 47, 12727 (1993).
27. L.D. Hicks and M.S. Dresselhaus, *Phys. Rev. B* 47, 16631 (1993).
28. G.D. Mahan and J.O. Sofo, *P. Natl. Acad. Sci. USA* 93, 7436 (1996).
29. A.I. Hochbaum, R.K. Chen, R.D. Delgado, W.J. Liang, E.C. Garnett, M. Najarian, A. Majumdar, and P.D. Yang, *Nature* 451, 163 (2008).
30. A.I. Boukai, Y. Bunimovich, J. Tahir-Kheli, J.K. Yu, W.A. Goddard, and J.R. Heath, *Nature* 451, 168 (2008).
31. T.E. Graedel, E.M. Harper, N.T. Nassar, P. Nuss, and B.K. Reck, *Proc. Natl. Acad. Sci. USA* 112, 4257 (2015).
32. P.E. Blöchl, *Phys. Rev. B* 50, 17953 (1994).
33. G. Kresse and D. Joubert, *Phys. Rev. B* 59, 1758 (1999).
34. G. Kresse and J. Furthmuller, *Phys. Rev. B* 54, 11169 (1996).
35. J.P. Perdew, K. Burke, and M. Ernzerhof, *Phys. Rev. Lett.* 77, 3865 (1996).
36. A.I. Liechtenstein, V.I. Anisimov, and J. Zaanen, *Phys. Rev. B* 52, R5467 (1995).
37. K. Parlinski, Z.Q. Li, and Y. Kawazoe, *Phys. Rev. Lett.* 78, 4063 (1997).
38. A. Togo, F. Oba, and I. Tanaka, *Phys. Rev. B* 78, 134106 (2008).
39. S. Grimme, *J. Comp. Chem.* 27, 1787 (2006).
40. T. Boker, R. Severin, A. Muller, C. Janowitz, R. Manzke, D. Voss, P. Kruger, A. Mazur, and J. Pollmann, *Phys. Rev. B* 64, 235305 (2001).
41. J. E. Sansonetti and W. C. Martin, "Handbook of Basic Atomic Spectroscopic Data" (NIST, 2009), http://www.nist.gov/pml/data/handbook/. Accessed 22 October 2015.
42. R.D. Shannon, *Acta Crystallogr. A* 32, 751 (1976).
43. G.K.H. Madsen and D.J. Singh, *Comp. Phys. Comm.* 175, 67 (2006).
44. Y. Wang, X. Chen, T. Cui, Y.L. Niu, Y.C. Wang, M. Wang, Y.M. Ma, and G.T. Zou, *Phys. Rev. B: Condens. Matter Mater. Phys.* 76, 155127 (2007).
45. C. Wang, Y.X. Wang, G.B. Zhang, and C.X. Peng, *J. Phys. Chem. C* 117, 21037 (2013).
46. K. Kaasbjerg, K.S. Thygesen, and K.W. Jacobsen, *Phys. Rev. B* 85, 115317 (2012).